





## Absence of the Great Whirl giant ocean vortex abates productivity in the Somali upwelling region

Fatma Jebri <sup>1</sup>✉, Meric Srokosz <sup>1</sup>, Dionysios E. Raitsos <sup>2</sup>, Zoe L. Jacobs<sup>1</sup>, Alejandra Sanchez-Franks<sup>1</sup> & Ekaterina Popova <sup>1</sup>

Somali upwelling is the fifth largest upwelling globally with high productivity, attracting tuna migratory species. A key control on the upwelling productivity is its interaction with one of the world's largest oceanic eddies, the Great Whirl inducing a strong downwelling signal. Here, we use satellite-derived observations to determine the Great Whirl impact on the extent of the upwelling-driven phytoplankton bloom. We find that following decreases in upwelling intensity, productivity has declined by about 10% over the past two decades. The bloom extent has also been diminishing with an abrupt decrease around 2006–2007, coinciding with an abrupt increase in the downwelling effect. Absent or weak Great Whirl leads to the occurrence of smaller anticyclonic eddies with a resulting downwelling stronger than when the Great Whirl is present. We suggest that 2006–2007 abrupt changes in the bloom and downwelling extents' regimes, are likely driven by Indian Ocean Dipole abrupt shift in 2006.

<sup>1</sup>National Oceanography Centre, Southampton, UK. <sup>2</sup>National and Kapodistrian University of Athens, Department of Biology, Athens, Greece.  
✉email: [fatma.jebri@noc.ac.uk](mailto:fatma.jebri@noc.ac.uk)

The Somali coastal region is unique in the global ocean, with the world's strongest coastal seasonal upwelling, the Somali upwelling, and a seasonal reversal in both atmospheric and oceanic circulation due to the monsoon winds<sup>1,2</sup>. The regional ocean circulation is dominated by the Somali Current (SC), the only major western boundary current in the world that reverses seasonally, which becomes one of the fastest open-ocean currents when flowing northward during the Southwest monsoon (May to September)<sup>1,3,4</sup>. The Somali upwelling is the largest upwelling system in the Indian Ocean and the fifth largest coastal upwelling in the world<sup>4,5</sup>. This exceptional upwelling occurs during the Southwest monsoon partly due to the cross-equatorial atmospheric flow between coastal East Africa and India, the southwesterly monsoon winds, which emerges in May and strengthens into the Findlater Jet (a low-level atmospheric jet), from June to September<sup>2,6–8</sup>. The southwest winds lead to a positive along-shore wind stress causing offshore Ekman transport<sup>9,10</sup>. Additionally, as the Findlater Jet extends across the Arabian Sea, the shear zone north of the jet exerts strong positive Wind Stress Curl (WSC) driving an Ekman pumping (open ocean upwelling) component along the Somali coast<sup>1,4,8,11,12</sup>. The wind-induced Somali upwelling component is estimated to be six times stronger than that in the most intense of the eastern coastal upwelling zones<sup>1</sup>.

The Somali upwelling brings up large amounts of nutrients ( $> 15 \mu\text{M}$ ) that approach regional deep-ocean values ( $20 \mu\text{M}$ ), leading to an enhanced phytoplankton bloom (bloom hereafter), in the ocean surface layer, and hence important productivity off the Somali coast<sup>3,13–15</sup>, ultimately sustaining rich fisheries<sup>1</sup>. Somali fishery resources are considered among the richest in Africa<sup>16,17</sup>. The potential yield of the small pelagic fish within the Somali Exclusive Economic Zone, evaluated at 75,000 metric tons, is one of the largest in the western Indian Ocean<sup>18</sup>. The large pelagics, including tuna and tuna-like species (e.g., yellow-fin, big-eye, skipjack) have high catch rates and are more lucrative despite being highly migratory<sup>15,17,19</sup>. The traditional fishing grounds are located off the Somali coast between  $5^{\circ}\text{N}$  and  $10^{\circ}\text{N}$  due to the dominant upwelling during the Southwest monsoon<sup>15,17,19</sup>.

Adding to the strong winds and rough sea state (high waves) during the Southwest monsoon are the fast-flowing SC and a series of associated anticyclonic eddies. In typical conditions, the northward flowing SC deviates from the coast at around  $4^{\circ}\text{N}$  and  $\sim 10^{\circ}\text{N}$  to flow eastward at the northern parts of the clockwise Southern Gyre (SG) and the Great Whirl (GW), a strong and large anticyclonic eddy<sup>3,4,14,20–22</sup>. The SC interacts also with other anticyclonic eddies such as the Socotra Eddy (SE), which develops to the east of the Socotra Island and is usually seen during mid-Southwest monsoon<sup>21,23</sup>. The GW is a major physical phenomenon during the Somali upwelling season. As the GW intensifies, it can reach 1000 m depth and transport an estimated 10–60 Sv of water, with speeds of  $0.1 \text{ m s}^{-1}$  on average<sup>21,24,25</sup>. The GW position is denoted by the position of the zero WSC contour line off the Somali coast<sup>2,25,26</sup>. The GW is generated to some degree by the remote forcing (downwelling Rossby waves) prior to the onset of the Southwest monsoon<sup>21,25</sup>. The westward propagation of downwelling Rossby and the negative WSC results also in an overall downwelling effect that includes other anticyclonic eddies as well as the GW<sup>27</sup>.

The GW has been extensively studied from a physics point of view<sup>21,22</sup> including its impact on the atmospheric boundary layer<sup>26</sup>. The GW has been mostly studied using satellite observations and models as it is difficult to study in-situ due to the piracy off the Somali coast<sup>28</sup>. The GW seasonal behaviour is thought to affect the ecosystem of the Arabian Sea<sup>29</sup>. However, it is still unclear what role the GW plays in the Somali upwelling

productivity (i.e., resulting bloom). Hitchcock et al.<sup>30</sup> investigated the fate of the upwelled waters along the northern edge of the GW from in-water surveys in 1995. They found that maximum Chlorophyll-a (Chl-a, a proxy for phytoplankton biomass) levels located at the northern edge of the GW are mainly the result of the rapid offshore advection of nutrients rich waters from the coastal upwelling. More recently, Dai et al.<sup>31</sup> used remote sensing and modelling approaches to examine the GW influence on Chl-a off the Somalia coast but only for 2017 and in terms of how phytoplankton can be imported into the interior of the GW. In this study, we propose to examine the role of the GW in the areal extent of the bloom along the Somali coast, focusing on the months of active upwelling (May–September), and using  $\sim 25$  years of satellite-derived ocean colour observations (1997–2021). Understanding the variations of the GW, including sudden changes or regime shifts, and how it interacts with the Somali upwelling productivity can help in the better management of fisheries.

Our study provides observational evidence indicating that the absence or smaller coverage of a giant ocean vortex, the GW, paves the way for other less dominant anticyclonic eddies to bring a stronger downwelling effect, decreasing the areal extent of the bloom for the past two decades. Moreover, we found that an abrupt change in the Indian Ocean Dipole (IOD) in 2006 has likely contributed to the regime changes seen in the extents of the bloom and the downwelling effect. We also show a decline in the bloom intensity (Chl-a levels) over the upwelling zone for the past two decades, following decreases in upwelling strength.

## Results

**Variability in upwelling and productivity.** In climatological Southeast monsoon conditions, both the Alongshore Wind Stress (AWS) magnitude and positive WSC (WSC+) intensify (reaching values  $> 0.16 \text{ N m}^{-2}$  and  $> 2.5 \cdot 10^{-7} \text{ N m}^{-2}$  per  $10^4 \text{ km}$  respectively) along the Somali coast (Fig. 1a and Supplementary Fig. S1a), compared to the Northeast monsoon, inducing upwelling<sup>4,9,10</sup>. The surface signature of the wind-driven Somali upwelling is visible in the satellite derived fields as cooler Sea Surface Temperature [SST] ( $< 26^{\circ}\text{C}$ ) associated with higher phytoplankton biomass ( $> 0.55 \text{ mg m}^{-3}$ ) and lower negative Sea Level Anomaly [SLA-] ( $< -0.05 \text{ m}$ ) relative to the surrounding waters (Fig. 1b–d). The productive upwelling signal is also reflected in the satellite derived elevated primary production ( $> 1.4 \text{ g C per m}^2 \text{ per d}$ ) compared to offshore areas (Fig. 1e). This upwelling signature is more marked at the SC  $\sim 10^{\circ}\text{N}$  wedge than that at  $\sim 4^{\circ}\text{N}$  which matches the SC behaviour (of stronger deviation at  $\sim 10^{\circ}\text{N}$  than  $\sim 4^{\circ}\text{N}$ ) (Fig. 1b–e, Supplementary Fig. S1b), further indicating its advective impact on the upwelling spatial extent<sup>4,15</sup>. The overall agreement of the climatological spatial distributions of both, the wind variables (i.e., high AWS and WSC+) and the upwelling effects (i.e., low SST, low SLA-, high Chl-a and primary production) along the coast (Fig. 1a–e, Supplementary Fig. S1a), strengthens the idea that the wind is an important forcing for the upwelling<sup>4,9,26,32</sup>.

The temporal variations of the upwelling parameters over the immediate “upwelling site” (Fig. 1a–e, black dashed contour, see “Methods” for details on the choice of region) reveal a strong seasonality (Fig. 1f–j, Supplementary Fig. S1c). From May to September (Southwest monsoon), increases in the ASW, WSC+, Chl-a and primary production (by up to  $\sim 0.2 \text{ N m}^{-2}$ ,  $\sim 4 \cdot 10^{-7} \text{ N m}^{-2}$  per  $10^4 \text{ km}$ ,  $0.7 \text{ mg m}^{-3}$  and  $0.6 \text{ g C per m}^2 \text{ per d}$  respectively) are observed associated with a decrease in SLA, becoming negative, and SST (by down to  $-0.2 \text{ m}$  and  $4.5^{\circ}\text{C}$  respectively) compared to the rest of the year (Fig. 1f–j, Supplementary Fig. S1c). The opposite effects are seen from

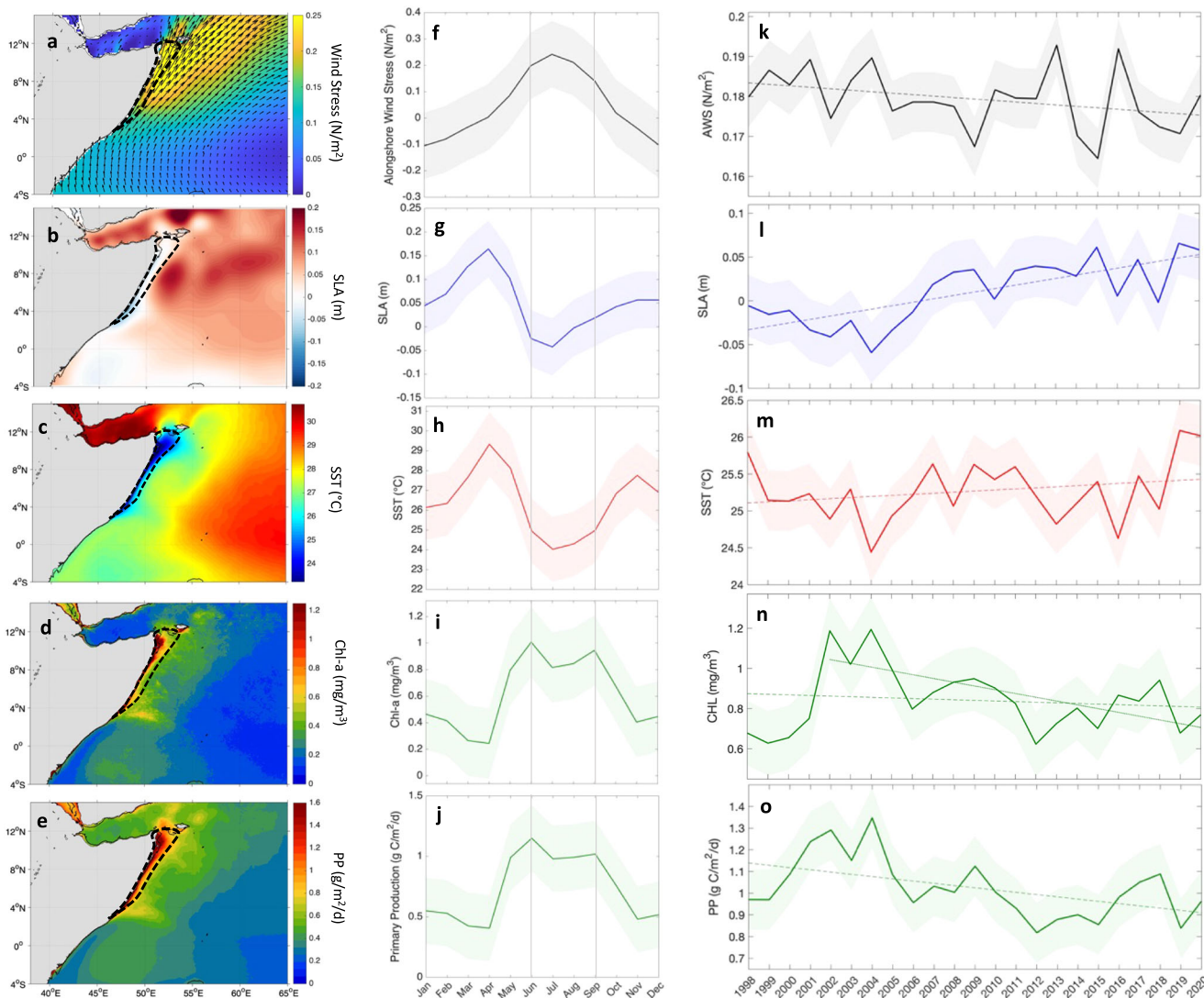


**Fig. 1 Seasonal and interannual variations of upwelling parameters along the Somali coast.** Climatological spatial distribution for June (representative of the Southwest monsoon) 1998–2020 of: **a** wind stress, **b** SLA **c** SST, **d** Chl-a, **e** PP. The dashed black contour line denotes the upwelling site area. **f–j** Seasonal cycles and **k–o** interannual (as averages of Southwest monsoon months) timeseries of upwelling parameters (AWS, SLA, SST, Chl-a, PP) over the upwelling site for 1998 – 2020. The light shaded areas in **f–j** represent  $\pm 2$  standard deviations from the climatology. The vertical lines in **f–j** mark the time of onset (June) and end of the Southwest monsoon (September). The dashed thin lines in **k–o** indicate the timeseries linear trend for 1998–2020. The dotted thin line in **n** indicate Chl-a linear trend for 2002–2020. The trend significance was calculated using Mann-Kendall test and t-test.

around December to March during the Northeast monsoon (Fig. 1e–h, Supplementary Fig. S1c). Interannually, the Chl-a Southwest monsoon (May–September) averages for 1998–2020 show some variations with more pronounced troughs (such as in 2019 and 2012) than peaks, but more importantly a continuous decreasing trend becoming significant from 2002 (Fig. 1n). Satellite-derived monthly primary production shows also significant decline from 1998 to 2020 (Fig. 1o), further demonstrating the low productivity trend over the upwelling site. The negative productivity trend is associated with significant increasing trends in SLA and SST and a negative significant trend in the AWS over the same period (Fig. 1k–o). Hence, it is likely that the Chl-a negative trend depicted for 2002–2020 (Fig. 1n) is on-going from 1998, especially that the Chl-a is highly negatively (positively) correlated to SLA (AWS) (Table 1) and the number of missing data is much higher in these first years of the continuous satellite ocean colour data record (cf. Supplementary Fig. S2b). No significant trend is seen in the WSC for Southwest

**Table 1 Pearson correlation coefficient ( $\Gamma$ ) significant at the 95% level between upwelling parameters over the upwelling site for September 1997 – June 2021.**

	Climatology	Jan-Dec	May
$\Gamma(\text{Chl-a, SST})$	-0.73	-0.66	-0.71
$\Gamma(\text{Chl-a, SLA})$	-0.77	-0.62	-0.52
$\Gamma(\text{Chl-a, WSC})$	0.81	0.67	0.51
$\Gamma(\text{Chl-a, AWS})$	0.83	0.70	0.53

monsoon averages of 1998–2020 (Supplementary Fig. S1d). Note that the rest of the analysis is carried out using Chl-a as it shows similar variability and trend to the primary production (Fig. 1d, e, i–j, n, o) in addition to both variables being highly correlated (0.8 with  $p$ -value  $< 0.05$ ), which suggests that Chl-a variations parallel those of primary production in the region (Supplementary Fig. S2a).

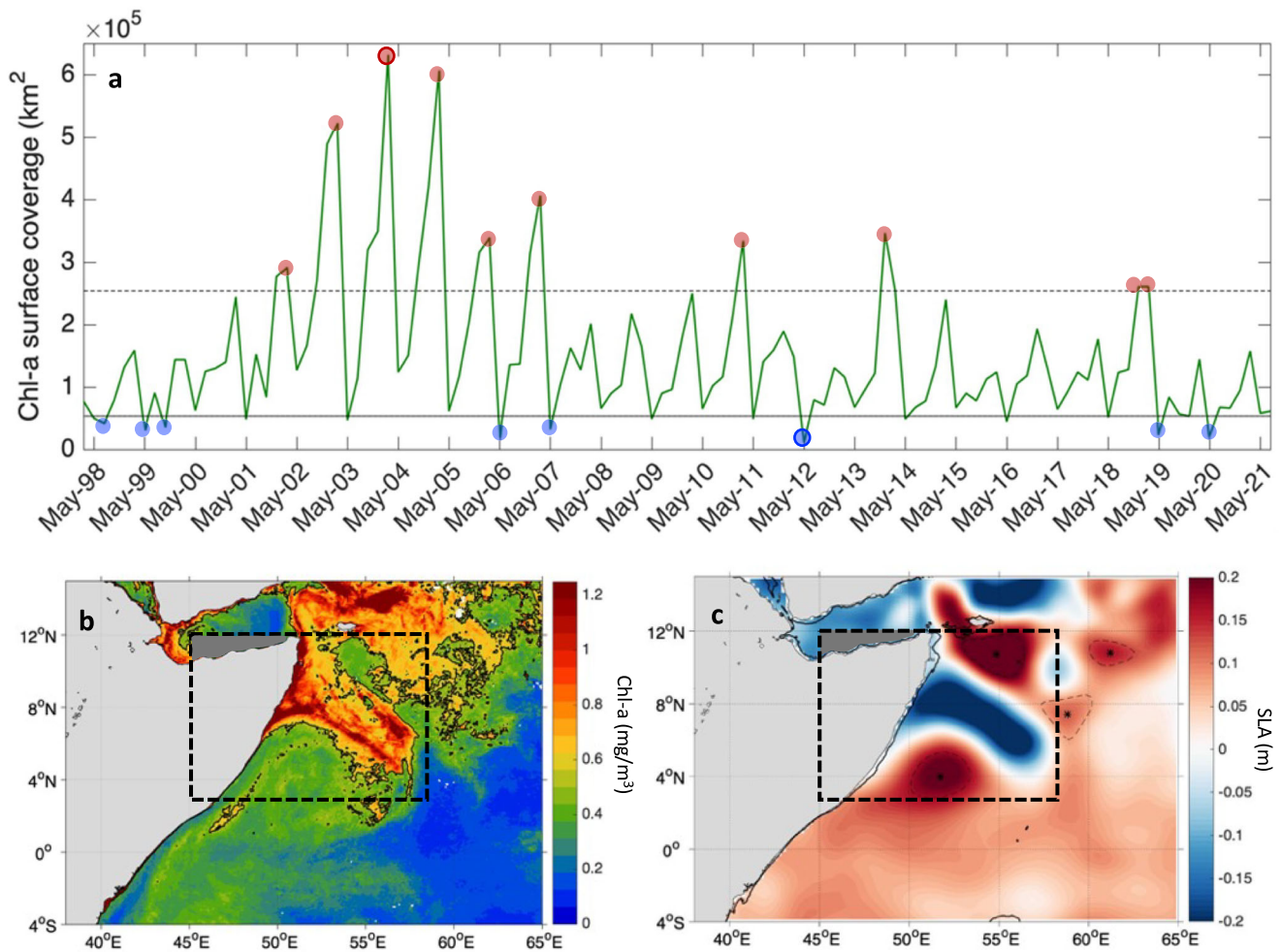


**Fig. 2** Bloom surface coverage along the Somali coast during the Southwest monsoon. **a** Monthly timeseries of the bloom (approximated by Chl-a) surface coverage (in  $\text{km}^2$ ) for May–September months of the period September 1997–June 2021 (in green). The values falling on the upper side of the  $253940 \text{ km}^2$  level, which is the mean of the surface coverage maxima timeseries (dashed horizontal line), indicate extreme large blooms and are highlighted in light red dots. The values falling on the lower side of the  $53333 \text{ km}^2$  level, which is the mean of the surface coverage minima timeseries (dotted horizontal line), indicate extreme small blooms and are highlighted in light blue dots. The most extreme large bloom (Sep-03) and smallest bloom (May-12) are further highlighted with dark red and dark blue circles, resp. Example of the **b** Chl-a (in  $\text{mg m}^{-3}$ ) and **c** SLA (in m) surface distributions for Sep 06. The black contour lines in **b** denotes the  $0.55 \text{ mg m}^{-3}$  Chl-a contour line. The dashed ellipses and black stars in **c** represent the edge and centre of anticyclonic eddies. The dashed black box in **b, c** indicate the location of the bloom box.

Chl-a shows high and significant positive (negative) correlations (of the order of 0.55–0.8 with  $p$ -values  $< 0.05$ ) with the AWS and WSC (SST and SLA) in the climatology, monthly means and Mays (the onset of the Southwest monsoons) for the nearly 24 years of observations (Table 1). This is in agreement with the wind driven upwelling along the coast. Although a good agreement is found for the seasonal cycle between the Chl-a, SST, wind forcing (AWS, WSC) and SLA (Fig. 1f–j, Supplementary Fig. S1c), at the interannual scale, considering all months or the Southwest monsoon months, the SLA parameter is the most closely linked to Chl-a over the upwelling site (Table 1). Previously, lowered SLA was also associated with the coastal upwelling along the Somali coast<sup>30,33,34</sup>. The fact that SST was not found to be the best upwelling indicator here is as expected. Indeed, the overall surface cooling off the Somali coast, although uniform, during the upwelling season is not entirely due to the upwelling effect and the changes in the net negative buoyancy flux and strong wind energy input contribute to the decrease in SST<sup>4</sup>. The AWS and WSC were found significantly correlated to Chl-a during the onset of the Southwest monsoon (Mays 1998–2021) (Table 1), indicating the triggering effect of the wind

forcing on the upwelling biological response. Reanalysis-based findings of a decreasing tendency in upwelling-favourable winds along the Somali coast<sup>10</sup> and in the Northwest Indian Ocean<sup>35</sup> agree with the significant negative trend in the AWS for 1998–2020 over the upwelling site (Fig. 1k). Moreover, a longer-term trend analysis of zonal wind stress, for 1958–2021 Southwest monsoon months, show a significant decreasing trend off the Somali coast (Supplementary Fig S3a).

The Southwest monsoon Chl-a maxima over the upwelling site reveals “high” and “low” with a similar order of magnitude for elevated values ( $> 0.55 \text{ mg m}^{-3}$ ), including their seasonal progression, while more pronounced changes are seen in the spatial extent of these higher Chl-a levels (Supplementary Fig. S4). The extreme spatial extents in the bloom (see “Methods” and Fig. 2 for details) are associated with the upwelling signal (as indicated by low SLA- coverage), developing at the inner edges of the SC, as it veers from and reverses back to the coast, and always bounded by the GW (Supplementary Figs. S7, S8 and Note 1). The latter can sometimes take the place of the SG and/or other anticyclonic eddies such as SE (Supplementary Fig. S7, S8 and Note 1) as previously modelled<sup>23</sup>. In agreement with our observations, the

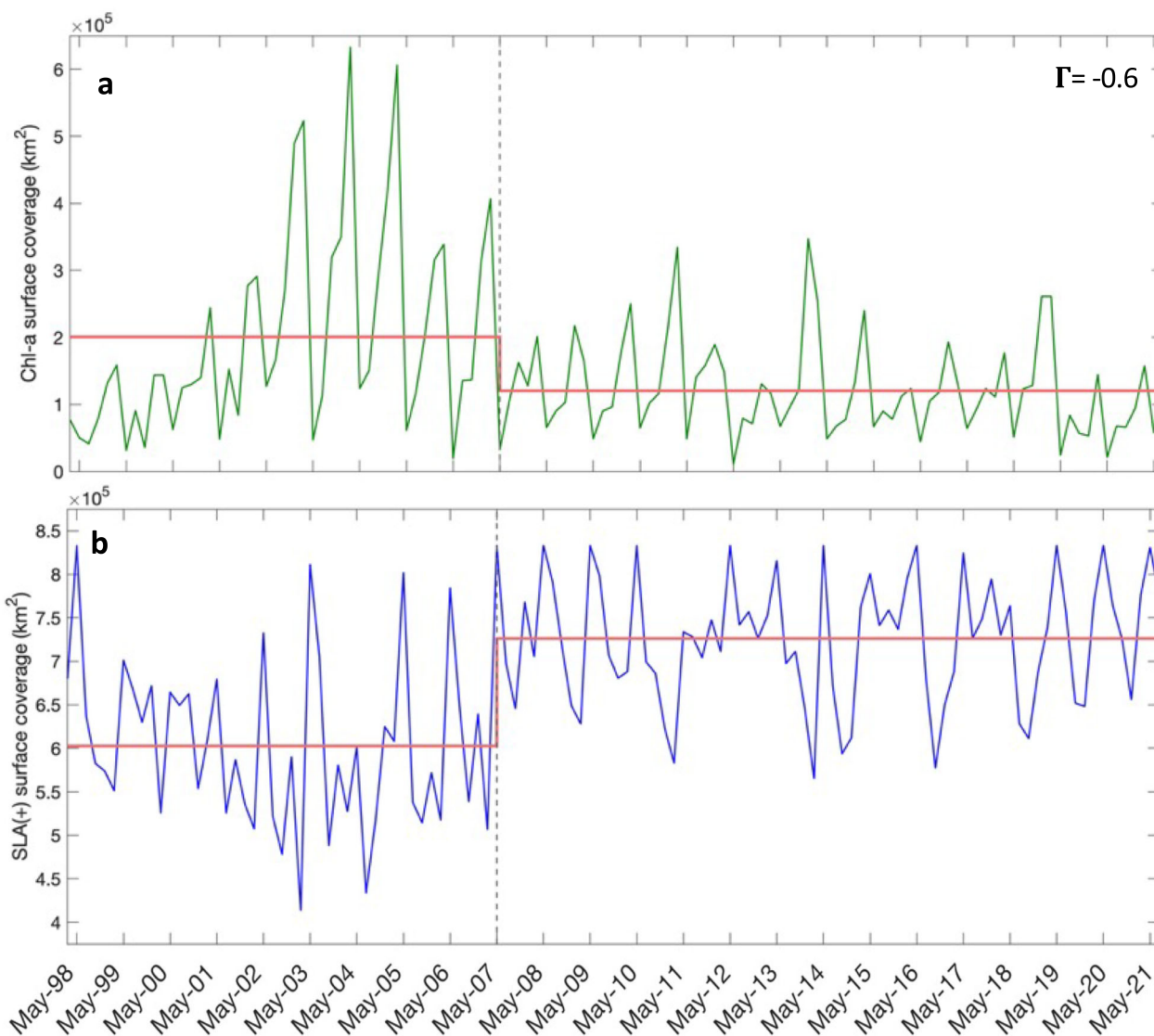


**Fig. 3 Regime shift of the bloom and downwelling extent for Southwest monsoons of September 1997–June 2021.** Monthly variations for May–Septembers 1997–2021 of the surface coverage (in km<sup>2</sup>) of **a** the Chl-a within the 0.55 mg m<sup>-3</sup> contour line versus **b** that of the SLA+ within the bloom box. The Pearson correlation coefficient ( $\Gamma$ ) significant at the 95% level is given in **a**. The solid red and dashed vertical grey lines in **a**) and **b**) represent the significant regime shifts (most significant change from the mean) and detected changepoint in the timeseries mean.

GW and SC flow along its northern arm have been shown to enhance the bloom extension off the coast<sup>30,31</sup>.

#### Abrupt change in the extents of the bloom, downwelling effect and the GW.

During the Southwest monsoons of 1997–2021, a significant negative correlation ( $-0.6$  with  $p$ -value  $< 0.05$ ) was observed between the extent of the bloom and positive SLA (SLA+) surface coverage, indicative of downwelling within the bloom region (Fig. 2). The bloom extent correlates also significantly ( $0.85$  with  $p$ -value  $< 0.05$ ) with SLA- surface distribution over the bloom region (Supplementary Fig. S9a), further confirming that the bloom extent during the Southwest monsoon is mainly associated with the upwelling signal. Additionally, a strong significant and positive correlation ( $0.7$  with  $p$ -value  $< 0.05$ ) was found between the SLA+ surface coverage inside the bloom region and the surface coverage of the non-bloom area (Supplementary Fig. S9b). These relationships suggest that downwelling factors, which include the GW and other anticyclonic eddies (e.g., Supplementary Figs. S7, S8), contrast the

areal extent of the bloom and the upwelling signal. Similar bloom scenarios can correspond to different conditions in size and position (closeness to the coast, north/south migration) of the GW which vary considerably from year-to-year and month-to-month (Fig. 2a, Supplementary Fig. S9c, d and Supplementary Note 2).

The bloom extent timeseries shows an overall decreasing tendency over the past two decades (2002–2021) similarly to the phytoplankton biomass downward trend over the upwelling site (Figs. 1n and 3a). The negative tendency in the bloom surface coverage is also associated with an increasing tendency in the SLA+ surface coverage inside the bloom box (Fig. 3). This suggests that the downwelling effect has been limiting the bloom extent over the past two decades. Visual inspection of the results in Fig. 3 suggests a possible change in regime around to 2007, so we test this by applying a changepoint analysis. The changepoint analysis reveals evidence of an abrupt shift in May 2007 after which the SLA+ (bloom) surface coverage increased above (decreased below) the overall mean with a  $1.23 \times 10^5$  km<sup>2</sup> ( $-0.08 \times 10^5$  km<sup>2</sup>) difference between 1998–2007 and 2007–2020 (Fig. 3).

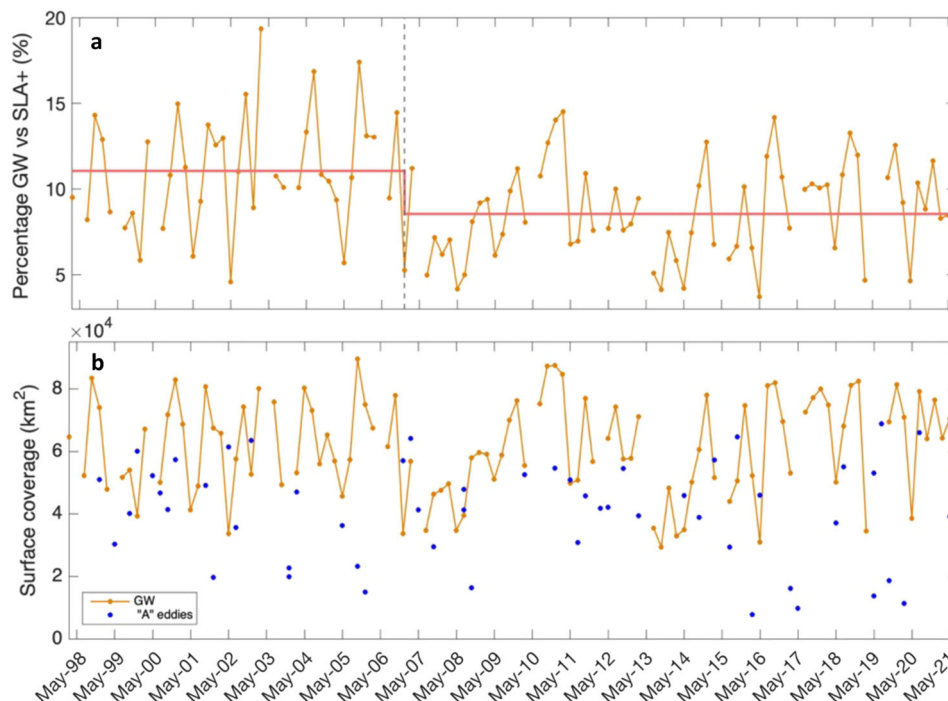


**Fig. 4** GW surface coverage variability and its contribution to the total downwelling effect over the bloom region. Monthly variations of the **a** the percentage of the GW in the SLA+ over the bloom region and **b** GW surface coverage (in  $\text{km}^2$ ) for May–September 1998–2021. The blue dots in **b** represent the surface coverage of other anticyclonic (A) eddies occurring with or without the GW over the bloom region. The solid red and dashed vertical grey lines in **a** represent the significant regime shifts (most significant change from the mean) and detected changepoint in the timeseries mean.

After the stepwise increase (decrease) of 2007, the extent of the SLA+ (bloom) remained at a high (low) regime without returning to its initial state (Fig. 3). The GW surface coverage contribution to this downwelling effect over the bloom region varies from at least  $\sim 4\%$  up to  $\sim 20\%$  and is on average 9.54% (with a standard deviation of 3.2%) for the full observational period (Fig. 4a). Although these extrema (i.e., the 4% and 20%) coincided with extremely large and small bloom extents (Figs. 2a and 4a), it does not imply that the greater (lower) the percentage of the GW in the SLA+ coverage the larger (smaller) is the bloom (i.e., their relationship is not straightforward). For example, the smallest GW percentage ( $\sim 5\%$ ) in the downwelling effect excluding May (where the GW do not always form and the upwelling season is at its very start), reached in July 2013, has an average bloom extent (Figs. 2a and 4a). Despite this nonlinear aspect, the GW has the largest impact in the SLA+ coverage among the anticyclonic eddies both in terms of surface coverage and number of occurrences. Indeed, the GW surface coverage is most of the time larger than that of any other anticyclonic eddy in the region (Fig. 4b). Additionally, the GW is present 88.14% during the Southwest monsoon months (104 out of 118 months) from September 1997 to June 2021, while other anticyclonic eddies take place (with or without the GW) only 43.22% of the Southwest monsoon months (51 out of 118 months) for the same period (Fig. 4b).

The GW percentage in the SLA+ coverage over the bloom box exhibits not only an overall decrease for 1998–2020 but also a significant changepoint (most significant change in the mean) from August 2006, after which a stepwise decrease by  $-2.51\%$  is evident without a return to the initial state (Fig. 4a). This might suggest that the GW is becoming less important, however, the GW surface coverage itself does not show a significant changepoint nor a trend for 1998–2020 indicating an overall stable regime (Fig. 4b). Although the GW surface coverage regime

itself is stable, extremes of large or small GW surface coverage are present (Fig. 4b). The extremes and overall regime of the GW surface coverage could be related to changes in the remote forcing (Rossby waves) prior to the start of the Southwest monsoon as this mechanism initiates the GW<sup>21,25,26</sup>. The GW changes could also be due to the alterations in the WSC and its zero line, which denotes the positions of the Findlater Jet and the GW, ultimately controlling the negative versus positive WSC distribution in the Arabian Sea<sup>2,25</sup>.

**Controls on the bloom extent regime.** By becoming increasingly important, the downwelling effect that is not due to the GW (e.g., other anticyclonic eddies) has been driving the increasing tendency in the downwelling effect (SLA+) over the bloom region for the past two decades (Fig. 5a). The non-GW downwelling effect surface coverage abruptly increased from its mean by  $1.34 \times 10^5 \text{ km}^2$  (significant changepoint detected in June 2007) between 1998–2007 and 2007–2020 (Fig. 5a). This suggests that the less dominant eddies (in terms of surface coverage and occurrence) are getting a more important effect and leading the SLA+ extent regime over the bloom region. Indeed, when the GW is absent or has a smaller coverage than other anticyclonic eddies, the generated downwelling effect is overall stronger (i.e., of a wider coverage) than when the GW is present with a high coverage (Fig. 5b). Thus, it is the absence of the GW (or its smaller coverage) that is more important for the bloom extent regime than its presence (which may enhance or bound the bloom extent (e.g., Supplementary Figs. S7, S8 and Note 1)). Both the SLA+ with absent/smaller GW coverage and that with a GW of higher coverage than other anticyclonic eddies have increased abruptly above their mean after 2007 by  $1.47 \times 10^5 \text{ km}^2$  and  $1.33 \times 10^5 \text{ km}^2$  respectively (significant changepoint detected in May 2007) without moving back to their initial state (Fig. 5b).

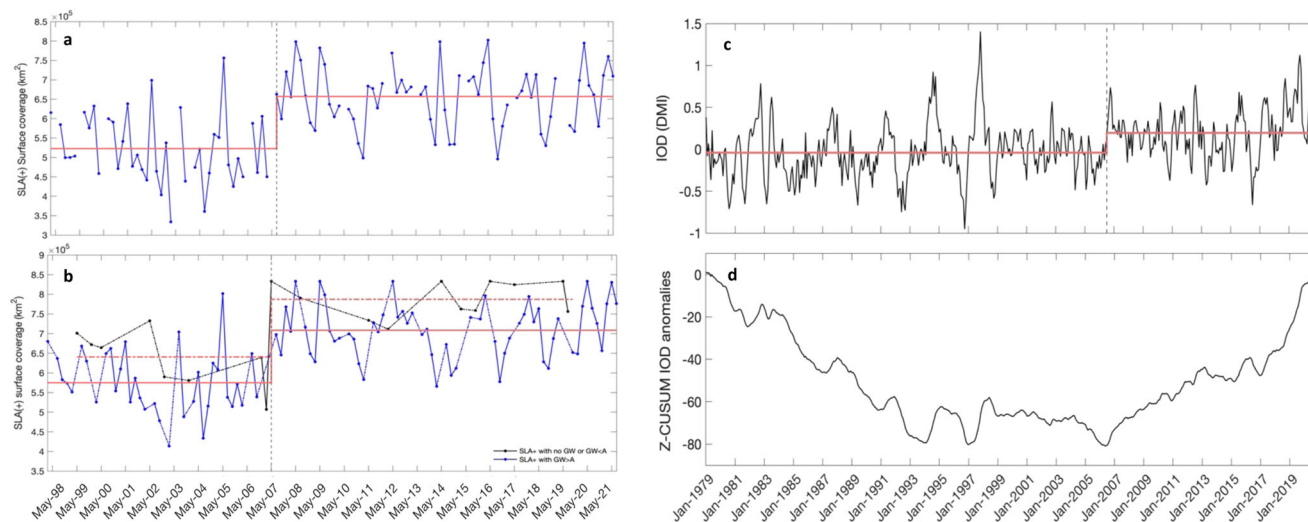


**Fig. 5** Changes in the non-GW versus the GW downwelling parts and Link to the IOD regime change. Monthly variations for May–September 1997–2021 surface coverage (in km<sup>2</sup>) of **a** the SLA+ of the non-GW downwelling effect over the bloom region; and of **b** the SLA+ with absent or lesser GW coverage than other anticyclonic eddies (A) (in black) versus that of the SLA+ with present GW of higher coverage than other A (in magenta). The part of the timeseries that are dashed in **b** indicate non available data. **c** Monthly IOD Dipole Mode Index (DMI) timeseries for 1979–2020. The solid red and dashed vertical grey lines in **a–c** represent the significant regime shifts (most significant change from the mean) and detected changepoint in the timeseries mean. **d** Cumulative sums of monthly IOD anomalies for 1979–2020. The Cumulative sums summarizes major changes by smoothing high frequency noise along the time-series (cf. Methods for more details). Increasing slopes represent positive temporal trends (periods with above average values) while decreasing slopes highlight negative temporal trends (periods with below average values), and horizontal segments indicate average conditions.

The abrupt shifts observed in the extents of the bloom and downwelling effect are all occurring around late Southwest monsoon 2006—early Southwest monsoon of 2007 (Figs. 3, 4a, 5a, b). It might be argued that this shift can be attributed to decadal variability since it is important in the tropical Indian Ocean<sup>36</sup>. Although the Chl-a record is not long enough, extending the SLA-based timeseries in Figs. 2b, 3a, 4a, b back to 1993 demonstrates further that the abrupt shift is indeed after 2006 and not just a phase of decadal variability (Supplementary Figs. S5 and S6). Given 2006–2007 is a strong positive Indian Ocean Dipole (IOD) year (e.g., Fig. 5c) and that the GW start time and lifetime were recently found correlated to the IOD, generating later, and lasting less than normal during strong positive IOD years<sup>37</sup>, we hypothesised the potential occurrence of an abrupt shift in the IOD possibly leading to the changes in the SLA+ and bloom coverages. The changepoint detection algorithm reveals a significant changepoint in the IOD 1979–2020 timeseries, indicative of a regime shift (most significant change in the mean), by 0.236 difference pre and post shift, from July 2006 (Fig. 5c). This is 1–11 months prior to the abrupt shifts observed in the bloom and downwelling effect extents displayed in Figs. 2a, 3, 5a, b. The application of normalized cumulative sums of anomalies (see “Method” for details) to the IOD timeseries confirms the timing of this abrupt shift (Fig. 5d). The cumulative sums of IOD anomalies show values consistently below the mean, producing an overall decreasing trend, prior to July 2006 and an opposite pattern after July 2006, mirroring the abrupt change detected from the changepoint analysis (Fig. 5c, d). Additionally, significant positive correlations (of the order of ~0.4 with  $p$ -value < 0.05) are found between the IOD and the total downwelling effect and non-GW downwelling effect over the bloom region (Figs. 3b, 5a) during the Southwest monsoons (May–Septembers) of 1998–2020. These results suggest that the increase in the downwelling effect (leading to a decrease in the bloom extent regime) over the bloom region around 2006–2007 is likely due to the abrupt shift in the IOD after July 2006. The 2006 shift observed here in the 1979–2020 IOD timeseries is about three

decades long. This is not totally surprising as, although the IOD is an interannual variability mode<sup>38</sup>, it has an important decadal to multi-decadal variability<sup>39,40</sup>. The changes in anomaly are also unlikely to be due to the warming of the Arabian Sea as it has been continuous since the early 1990s<sup>41</sup>.

Although most past studies failed to demonstrate strong links between the IOD, as a climate variability mode intrinsic to the Indian Ocean, and the GW development or intensity<sup>21,24</sup>, the recent work by Dai et al.<sup>37</sup> showed that the GW start time (lifetime) is significantly positively (negatively) correlated to the IOD during September–November months. The authors demonstrated also that anomalous northeasterly wind and Rossby waves during strong positive IOD years result in a late generation time and short lifetime of the GW<sup>37</sup>. Here the timing of the abrupt shift found in the IOD is few months prior to the shifts detected in the GW percentage in the SLA+ over the bloom region and the other downwelling effect metrics (cf. Figs. 3, 4a, 5). This delayed effect is coherent with Beal and Donhue<sup>21</sup> suggestion of the formation of the GW being the result of remote forcing transmitted by Rossby waves before the onset of the Southwest monsoon. Our results support further Dai et al.<sup>37</sup> proposal that the IOD might influence the GW variability.

It is also acknowledged that the Rossby waves propagation emanating from both the Northwest Tropical Indian Ocean (NTIO) (as reflected coastal trapped Kelvin waves) and from the South Tropical Indian Ocean (STIO) (as reflected equatorial Kelvin waves) play a key role in the formations of strong positive IODs and the GW<sup>37,42</sup>. Positive IODs were also associated with combined downwelling Rossby waves (as reflected equatorial Kelvin wave and direct wind induced), which lead to thermocline deepening and sustained anomalously warm SST in the Western equatorial Indian Ocean<sup>43</sup>. These Rossby waves are excited by changes in the anticyclonic Wind Stress Curl Anomalies (WSCA)<sup>44–46</sup>. A time-space diagram along the latitude line 9°N of SLA shows a westward movement, indicative of Rossby wave propagation towards the Somali region<sup>44</sup>, with more positive SLA starting to exceed 0.2 m after 2006 (Fig. 6a, b, green contours).

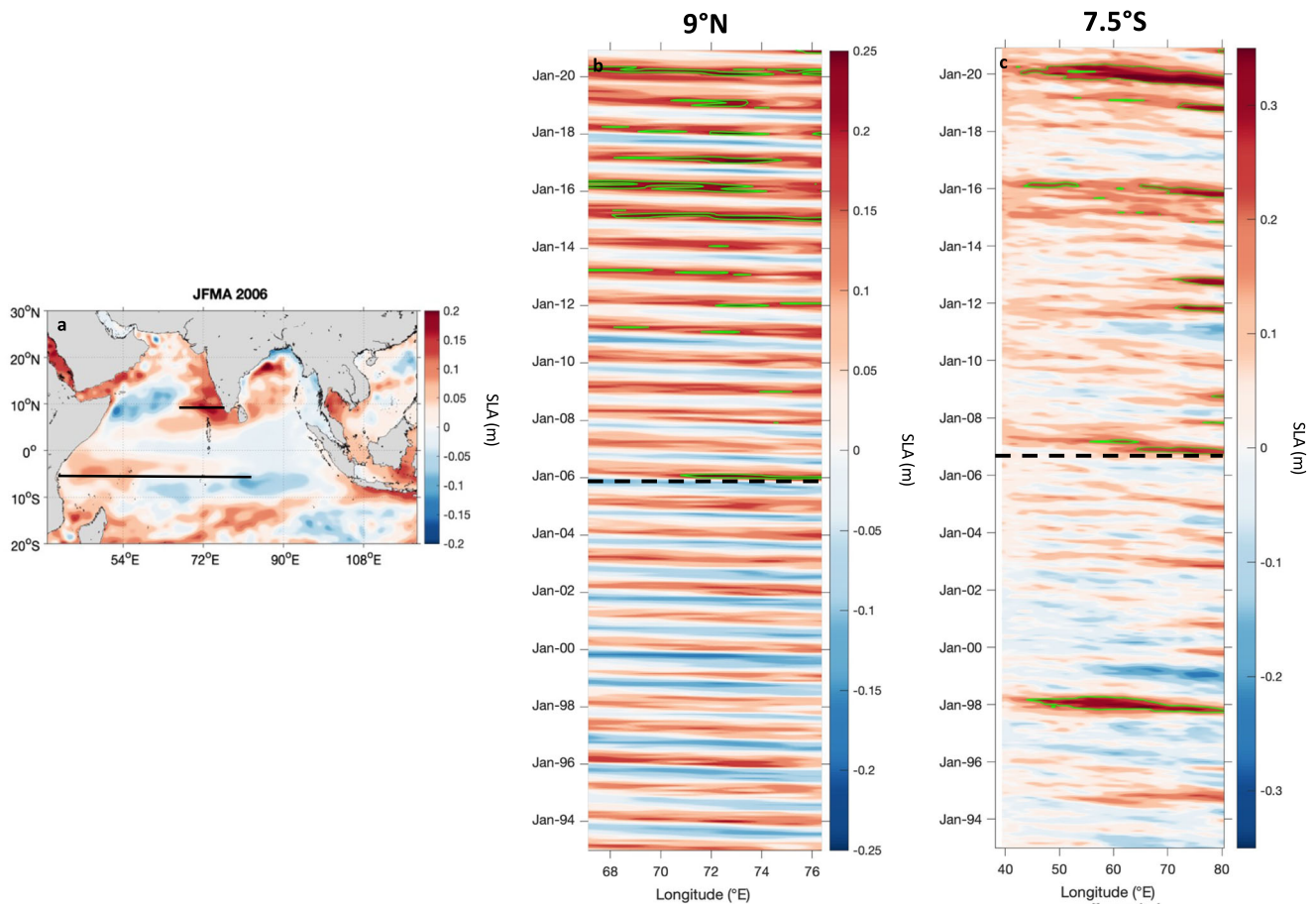


**Fig. 6** Westward propagation of Rossby waves as depicted from SLA signal in the NTIO and STIO over the period 1993–2020. **a** SLA (in m) for January–April (JFMA) 2006 over the Indian Ocean and 9°N and 7.5°S latitude lines along which **b**, **c** time-space diagram of SLA are derived between 67–76.5°E and 38–81°E respectively. The green lines in **b**, **c** highlight the SLA 0.2 m contours and the dashed black lines indicate the change in SLA behaviour from 2006.

This apparent shift in behaviour in the downwelling Rossby waves propagation in the NTIO is associated with change in the anticyclonic WSCA detected along the 7.5°N latitude line off India west coast with higher values exceeding  $0.5 \text{ N m}^{-2}$  per  $10^4 \text{ km}$  after 2006 (Fig. 7a, b). We also detect a change in the Rossby waves propagation in the STIO along 7.5°S with more frequent positive SLA higher than 0.2 m after 2006 (Fig. 6c, green contours), except for 1997–1998 which is likely due to the exceptional conditions of 1997–1998 super El Niño<sup>47–49</sup>. Indications of change in the anticyclonic WSCA in the STIO can be observed along 5°S off Sumatra from 2006 with more positive WSCA higher than  $1.12 \text{ N m}^{-2}$  per  $10^4 \text{ km}$  (Fig. 7c, green contours). The changes in the WSCA in the NTIO and STIO can be attributed to alterations in the Indian Ocean Walker circulation via anomalous easterlies over the equator and southeasterlies off Sumatra which represent the first atmospheric triggers of the IOD<sup>45,46,50,51</sup>. Other studies have linked the Rossby waves propagation in both the NTIO and STIO to changes in the thermocline in the tropical Indian Ocean which in turn alter the SST leading to the IOD temporal signature<sup>43,46,51,52</sup>. Evidently, the SST changes would in turn affect the easterlies and southwesterlies, but investigating this internal feedback loop requires a separate modelling study in future research. Our results of changes in the Rossby waves propagation and the WSCA around 2006 in the NTIO and STIO, supports the mechanistic link between the IOD, the GW and the upwelling productivity off the Somali coast. Although the 2006–2007 positive IOD is not the

strongest positive IOD event on record, it was unique because it marked the start of a rare manifestation of three consecutive positive IODs<sup>53,54</sup>, followed by an escalating occurrence of positive IODs in recent years as shown by Albert et al.<sup>55</sup> (their figure 13). In terms of upwelling intensity, the decrease in the zonal wind stress during the Southwest monsoon (1958–2021) off the Somali coast post 2006 (Supplementary Fig. S3b) suggests that the local forcing has also changed after 2006.

## Discussion

The results presented in this study highlight the key role ocean vortices can play in regulating the productivity of one of the world's largest upwelling systems and demonstrate how atmospheric (e.g., wind) or climate mode (e.g., IOD) mechanisms could influence it. With the decline in the phytoplankton biomass over the upwelling zone for the past two decades, following decreases in upwelling strength and wind forcing, an investigation into the wind-biological interactions, using ocean–atmosphere–biogeochemistry coupled models could provide further insights. How the upwelling strength might affect deoxygenation occurring in nearby regions of the Arabian Sea<sup>8</sup> is also yet to be examined in future research. Our results demonstrate also that the bloom extent experienced an abrupt decrease associated with an abrupt increase in the downwelling coverage after 2007, linked to an abrupt increase in the non-GW downwelling effect in 2006–07. More specifically, when the GW is absent or has a smaller areal



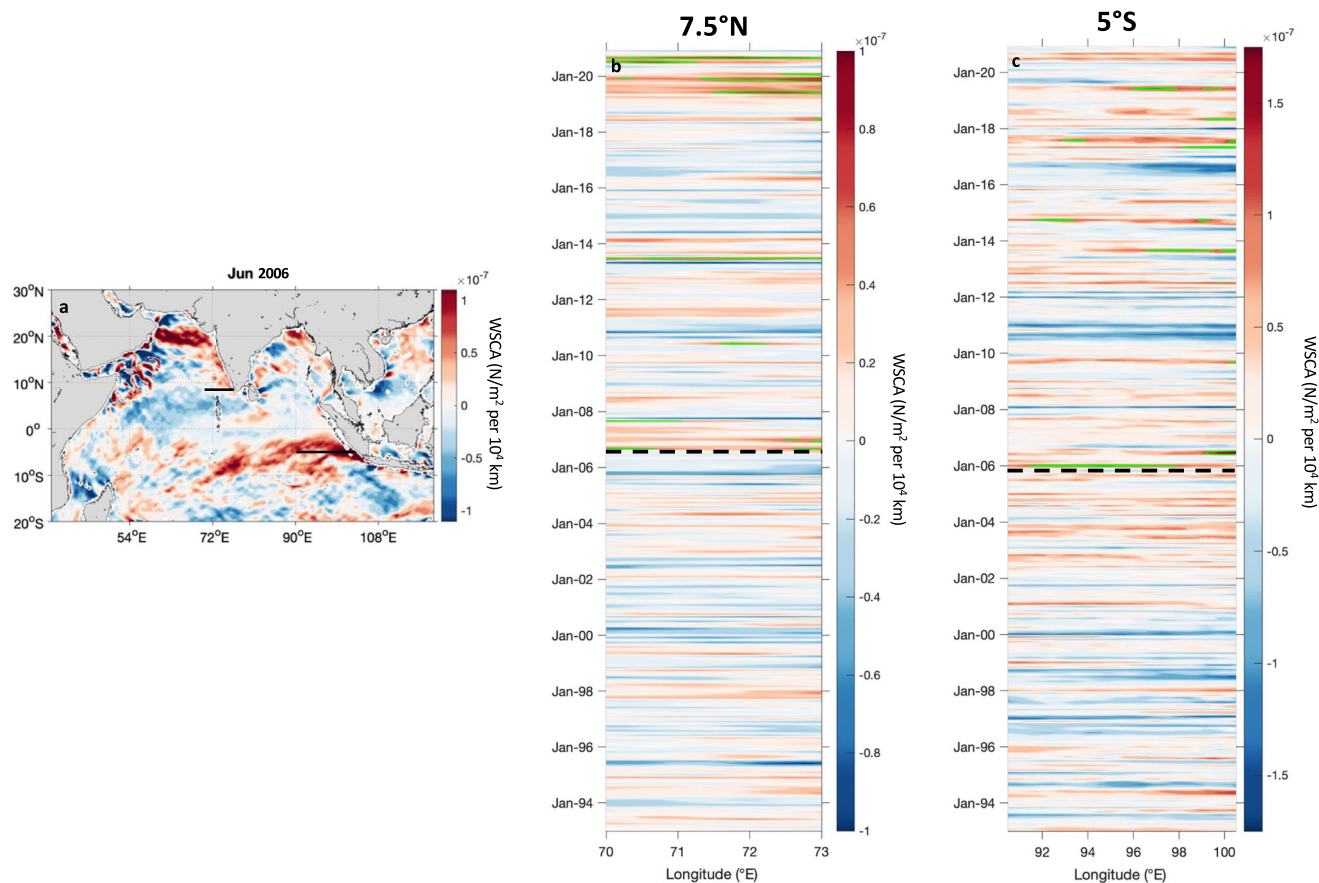


**Fig. 7** Changes in WSCA in the NTIO and STIO over the period 1993–2020. **a** WSCA ( $\text{N m}^{-2}$  per  $10^4$  km) for June 2006 over the Indian Ocean and  $7.5^\circ\text{N}$  and  $5^\circ\text{S}$  latitude lines along which (b–c) time-space diagram of WSCA are derived between  $70\text{--}73^\circ\text{E}$  and  $90.5\text{--}100.5^\circ\text{E}$  respectively. The green lines in **b** highlight the WSCA  $0.5 \text{ N m}^{-2}$  per  $10^4$  km contours and those in **c** the WSCA  $1.12 \text{ N m}^{-2}$  per  $10^4$  km contours. The dashed black lines indicate the change in WSCA behaviour from 2006.

coverage than other less dominant anticyclonic eddies, the generated downwelling effect is overall stronger than when the GW is present with a high coverage, limiting further the bloom extent. Therefore, we conclude that the absence of the GW is more important for the bloom extent regime than its presence. Simply put, the GW absence leads to a stronger downwelling impact on the bloom extent than when it is present; and on the long term this behaviour affected the bloom extent regime. The abrupt changes in the extents of the bloom and downwelling regimes observed around 2006–07, are likely due to the abrupt shift in the IOD detected in July 2006. Changes in other remote large-scale influences such as El Niño Southern Oscillation, may produce changes that affect nutrient supply to the upwelling waters<sup>56</sup> and remain to be investigated.

The declining productivity, seen here in both the bloom intensity and extent and their controls, provides a foundation for future research on the productivity regime changes using climate model projections. This is particularly important because the Southwest (Indian summer) monsoon, which is when the Somali upwelling occurs, has been identified as one of the climate system's tipping points<sup>57</sup>. The fate of both the GW and anticyclonic eddies interacting with the upwelling productivity need to be examined in such scenarios with a disruption of the monsoon systems in the future climate projections. This, in addition to continuous monitoring of environmental conditions using satellite observations, could provide useful information on potential low productivity scenarios, and in turn, fisheries, which are of socio-economic importance to the local communities and stakeholders in Somalia and the northwestern Indian Ocean.

## Methods

**Satellite derived data.** We use monthly reprocessed satellite-derived *Chl-a* data available from the Ocean-Colour Climate-Change Initiative project (OC-CCI version 5<sup>58</sup>, <http://www.esa-oceancolour-cci.org/>), at a spatial resolution of 4 km. This dataset is the most consistent timeseries of multi-satellite (MODIS-Aqua, SeaWiFS, MERIS and VIIRS) global ocean colour data<sup>56</sup>. The *Chl-a* monthly composites span the period September 1997 to June 2021. They are used to examine the *Chl-a* variability seasonally and interannually off the Somali coast. Although the OC-CCI processing applies a multi-chlorophyll algorithm approach<sup>59</sup>, satellite-derived *Chl-a* could still be overestimated in coastal and/or shallow waters (generally shallower than 30 m<sup>60</sup>). The bottom reflectance issues, and suspended material (such as sediments and dissolved organic matter) present in shallow optically complex waters which may lead to high water leaving radiance, and in turn, an overestimation of the correction term<sup>61</sup>. However, these high *Chl-a* values in coastal/shallow areas are not necessarily erroneous. They could reflect the highly productive coral reef zones, or chlorophyll-rich detritus regions enhancing phytoplankton growth near the coast<sup>62,63</sup>. Regardless, the Somali region consists mainly of deep oceanic waters including the “upwelling site” region (see Section 4.4 for details and Fig. 1a–e, black dashed contour) where 98.15% (87%) of the data represent waters deeper than 30m (100 m).

The satellite-derived primary production data used here are processed by ACRI-ST based on the Copernicus-GlobColour processor and retrieved from the Copernicus Marine Environment Monitoring Service (CMEMS) (<http://marine.copernicus>).

[eu/services-portfolio/access-to-products/](http://eu/services-portfolio/access-to-products/)). This is a global multi-satellite product available monthly with a horizontal resolution of 4 km and spanning the period September 1997 to January 2023. Primary production was calculated using Antoine and Morel Algorithm<sup>64</sup>, and uses satellite-derived ocean colour products (merged Chl-a, Photosynthetically Active Radiation [PAR]<sup>65</sup> and Kd(PAR)), SST and a mixed layer depth climatology, estimated based on de Boyer Montegut<sup>66</sup> definition. The primary production algorithm is validated globally against in situ data<sup>67</sup>.

We utilize altimetry-derived SLA and absolute geostrophic currents processed by CLS (previously by AVISO (Archiving, Validation and Interpretation of Satellite Oceanographic Data)) and distributed by CMEMS (<http://marine.copernicus.eu/services-portfolio/access-to-products/>). These multi-satellite (Jason-3, Sentinel-3A & 3B, HY-2A, Saral/AltiKa, Cryosat-2, Jason-2, Jason-1, T/P, ENVISAT, GFO, ERS1/2) dataset are daily composites gridded at 25 km spatial resolution from the delayed time DUACS\_DT2018 version and spanning the period 1993–2021. The SLA product is referenced to a twenty-year (1993–2012) mean<sup>68</sup>. Only the period September 1997–June 2021 is considered, to match the satellite Chl-a data. The SLA data is used to characterise the upwelling surface signature and eddies. The geostrophic currents are used to examine the surface circulation. To overcome the geostrophic limitation near the equator, the geostrophic current field product applies the  $\beta$  plane approximation<sup>69</sup>. Satellite altimetry data can be impacted by the sensor contamination near the coast<sup>70</sup>. However, our region (Fig. 1a–e) comprises mainly open waters. The product version has also a reduction in error on geostrophic currents in coastal zone by >15%<sup>71</sup>.

The reprocessed SST Met Office Operational-Sea-Surface-Temperature-and-Sea-Ice-Analysis (OSTIA) product, acquired from CMEMS (<http://marine.copernicus.eu/services-portfolio/access-to-products/>) is used. This multi-satellite global SST dataset is provided daily at 5 km spatial resolution from 1981 to 2021. Monthly SSTs are computed for the same period as Chl-a (September 1997–June 2021).

**Wind parameters.** We use the ERA-5 reanalysis 10 m zonal and meridional winds produced by the European Centre for Medium-Range Weather Forecasts (ECMWF). This dataset is made available by the Climate Data Store (CDS) (<https://cds.climate.copernicus.eu/cdsapp#!/dataset/reanalysis-era5-single-levels-monthly-means?tab=overview>; Hersbach et al.<sup>72</sup>) at a 25 km spatial resolution and as monthly means from 1979 to present. However, only the period September 1997 to June 2021 is used to match the Chl-a time coverage. We calculate the AWS along the Somali coast using the zonal and meridional wind components. The wind stress fields are computed using the Gill<sup>73</sup> equation:

$$\tau = \rho_a C_d |v|v \quad (1)$$

where  $\tau$  and  $v$  are the wind stress and wind vectors, respectively.  $\rho_a$  is the air density ( $1.2 \text{ kg m}^{-3}$ ) and  $C_d$  is the drag coefficient determined following *Large and Pond* (1981) equation:

$$C_d = (0.49 + (0.065 U_{\text{wind}}))10^{-3} \quad \text{if } U_{\text{wind}} \geq 11 \text{ ms}^{-1} \\ C_d = 0.0013 \quad \text{if } U_{\text{wind}} < 11 \text{ ms}^{-1} \quad (2)$$

where  $U_{\text{wind}}$  is the winds at 10 m. The coastal AWS provides information on the Ekman transport wind-driven upwelling, which bring nutrient-rich waters towards the surface. This variable has been previously used to provide estimates on upwelling intensity, especially in regions around the Equator such as the Somali region where Ekman transports diverge (e.g.,<sup>9</sup>). We also examine the WSC which is a sign of vertical pumping and proportional to the vertical velocity. WSC induced upwelling along

the Somali coast is known to be important during the start of the Southwest monsoon<sup>4,26</sup>. WSC+ indicates ocean surface divergence forcing waters upward (upwelling - Ekman pumping) in the northern hemisphere<sup>10,32</sup> and vice versa for negative WSC. The WSC is computed using the wind stress fields in the following equation:

$$\text{WSC} = \frac{\partial \tau_y}{\partial x} - \frac{\partial \tau_x}{\partial y} \quad (3)$$

where  $\tau_x$  and  $\tau_y$  are the zonal and meridional components of the wind stress (cf. Equation (1)) and  $x$  and  $y$  are the zonal and meridional dimensions.

We also use monthly zonal wind stress for 1958–2021 calculated from the Japanese 55-year atmospheric reanalysis<sup>74</sup> based surface dataset (JRA55-do)<sup>75</sup> to investigate the local wind forcing affecting the upwelling intensity at a longer term. This dataset is available at a spatial resolution of 55 km and on a 3 h basis.

**IOD data.** Monthly IOD Dipole Mode Index (DMI) timeseries for 1979–2020 is used here. This IOD timeseries is the HadISST v1.1 version downloaded from <https://psl.noaa.gov/data/timeseries/DMI>.

**Eddy detection algorithm and GW identification.** We use an automated eddy detection algorithm to determine the position and surface coverage of the GW off the Somali coast. Automated eddy detection algorithms can be based on physical quantity, flow geometry characteristics or they can be hybrid, which is a combination of the two former categories<sup>76</sup>. Here, we apply a hybrid method where SLA (as a physical parameter) is used to spot eddies and streamlines (as flow geometry characteristics) are utilized to determine eddy edges. SLA is conventionally used in identifying and tracking mesoscale eddies in ocean regions deeper than 200m<sup>77,78</sup>. Since streamlines associated with eddies are parallel to SLA contours under the geostrophic assumption<sup>78,79</sup>, closed SLA contours are considered here as a proxy for closed streamlines.

The hybrid eddy-identifying method used in this study was employed by Chaigneau et al.<sup>80,81</sup>, Zhang et al.<sup>78</sup>, Chelton et al.<sup>81</sup> and Xu et al.<sup>82,83</sup>. The algorithm identifies eddies by finding their centre and edges (i.e., outermost closed contour of SLA which defines a compact structure)<sup>78,83</sup>. The centre of a possible eddy is determined by looking for the mass centre of an innermost closed SLA contour. All closed contours, surrounding the centre, with their SLA values changing monotonously outward from the centre are identified. The outermost closed SLA contour defines the eddy edge<sup>78</sup>. The following eddies-identifying criteria, adapted from Xu et al.<sup>82,83</sup> and Zhang et al.<sup>78</sup> are considered: (1) Eddies amplitude, defined as the SLA difference between the centre (i.e., SLA extremum in the eddy interior) and the edge (i.e., value of the outermost closed SLA contour), is at least 3 cm. The choice of this  $\pm 3$  cm threshold is due to the altimeter observation error (2–3 cm), so that eddies with amplitudes less than 3 cm are excluded. (2) The zonal and longitudinal extent of the eddy area (i.e., area enclosed by the eddy edge) are at least  $0.5^\circ$  long. (3) The distance between two arbitrary points on the SLA contour should not exceed 400 km. (4) The eddy centre is taken as the midpoint between the centroid of the area within the eddy edge and the location of the SLA extremum, in order to minimize the error. (5) Eddies radius, defined as the radius of a circle with the same area as that of the eddy, should be larger than 45 km. This threshold is established due to the spatial resolving capability of the altimetry data. (6) Data in the equatorial band (i.e., with latitudes in  $\pm 3.5^\circ \text{N}$  range) are disregarded as the Coriolis

parameter approaches zero there, lowering the performance of the eddy-identifying method.

The eddy detection algorithm is an adapted version of the MATLAB subroutine SimpleEddyDetection.m that is available freely online<sup>84</sup>. The algorithm takes as inputs the longitude, latitude, SLA (in m) and date (year, month, day) of the SLA measurements. The output consists of a structure array with the properties of detected eddies: polarity (i.e., cyclonic or anticyclonic), centre, amplitude, radius and edge (defined by the largest closed sla contour). To distinguish the GW from the rest of eddies returned by the algorithm, only the anticyclonic eddies that fall within the GW centre known latitudinal and longitudinal extent (i.e., from 4 to 12°N and from 45 to 56°E)<sup>22</sup> are kept. Then the GW locations (i.e., centre and edge) found by the algorithm are plotted superimposed to the SLA monthly maps and to the WSC zero contour line over the full observation record (e.g., Supplementary Figs. S7, S8). In fact, the WSC zero contour line is always tangent to the GW edge<sup>21,26</sup>. This condition is used to validate the GW location. It is also visually tracked from the start to the end of the Southwest monsoons of the full observational record to further check the identified location.

There have been different approaches and algorithms to detect and track the GW based on streamlines (approximated by SLA), surface currents or Absolute Dynamic Topography<sup>21,22,26,81,85–87</sup>. Although the choice of the method impacts the GW metrics, including its surface coverage (e.g., Melzer et al.<sup>22</sup> method led to the largest estimation of the GW size), the GW characteristics obtained here agree with a number of these previous investigations<sup>21,22,87</sup>. Our approach was also verified using the WSC zero contour line and a visual comparison of the detected GW and its signature in other ocean fields (e.g., surface currents and Chl-a).

**Choice of region for analysis of temporal upwelling parameters.** We select an area representative of the immediate “upwelling site” (Fig. 1a–e, black dashed contour), based on the climatological spatial distribution of the upwelling triggers (i.e., high WSC+ (> 2.5 N m<sup>-2</sup> per 10<sup>4</sup> km) and high wind speed, Fig. 1a, Supplementary Fig. S1a) and effects (i.e., cool SST (< 26 °C), low SLA- (< -0.05), high Chl-a (> 0.55 mg m<sup>-3</sup>) and primary production (> 1.4 g C per m<sup>2</sup> per d), Fig. 1b–e) along the Somali coastline.

**Bloom surface coverage metric.** To characterize the surface coverage of the Somali bloom (Somali upwelling productive signal), we used a box, called hereafter “the bloom box” (Fig. 2), in a similar fashion to how other large blooms in the Indian Ocean were described such as the Southeast Madagascar bloom<sup>88,89</sup>. Although the Somali upwelling productive signal has a well-defined shape in the climatological mean with two wedges at ~4°N and 10°N (Fig. 1b–e, Supplementary Fig. 1b), the inter-annual variations of its geographical extent can differ considerably from the climatology (e.g., Supplementary Figs. S7, S8). Due to this substantial spatial variability, we tested different Chl-a contour lines (0.45, 0.55, 0.6 and 0.65 mg m<sup>-3</sup>) comparing them subjectively by visual analysis to the spatial distribution SLA-, which is indicative of upwelling<sup>26,30</sup>. The pixels with higher Chl-a than a threshold value should match overall the spatial extent of the SLA- (e.g., Fig. 2b, c). The 0.55 mg m<sup>-3</sup> Chl-a contour is selected as it was found to be the most representative of the spatial extent of the Somali phytoplankton bloom for each month of the Southwest monsoon over the ~24 years of observations. The bloom surface coverage is then computed by summing the surface coverage (in km<sup>2</sup>) of all the pixels (each representing

4\*4 km<sup>2</sup>) within this threshold value (0.55 mg m<sup>-3</sup> Chl-a contour) and inside the bloom box.

This bloom spatial distribution metric is based on a statistical method with empirical thresholds, similar to upwelling productivity delimitation approaches used in the WIO<sup>90</sup>. Less empirical methods such as the recent automatic detection of upwelling in the WIO developed by Hammond et al.<sup>91</sup>, so called “upwelling watch” is aimed for operational purposes and upwelling detection only. Here, our goal was to delineate the spatial extent of both upwelling productivity and the downwelling effect.

Using the bloom surface coverage metric, extremely “Larger” (“smaller”) extension events can be identified as Chl-a surface coverage values falling on the upper (lower) side of a threshold defined by the mean level of their maxima (minima) timeseries, here corresponding to 2.54 10<sup>5</sup> km<sup>2</sup> (0.53 10<sup>5</sup> km<sup>2</sup>) (Fig. 2a, dashed and dotted horizontal lines).

**Changepoint detection analysis.** To confirm the existence of statistically significant abrupt changes in the SLA+ and Chl-a surface coverage timeseries, we apply a changepoint detection algorithm, the findchangepts MATLAB sub-routine. This algorithm is based on the Pruned Exact Linear Time (PELT) method, an optimal segmentation algorithm, which finds the optimal number of changepoints and has a linear computational cost, leading to accurate segmentation of the data<sup>92,93</sup>. The PELT method is combined with the modified Bayesian information criterion (MBIC) as the penalty function to select an optimal number of changepoints<sup>93</sup>. The approach is effective in differentiating abrupt changes from trends and memory in timeseries<sup>93</sup>. Full details of the algorithm can be found in Beaulieu & Killick<sup>93</sup> and references therein. This method was proven to perform better than some commonly used approaches for the detection of abrupt changes in climate timeseries<sup>93</sup>, such as, the sequential *t*-test analysis of regime shifts approach by Rodionov<sup>94</sup> and the Bayesian linear regression multiple changepoint-detection method by Ruggieri<sup>95</sup>. Additionally, Rodionov<sup>94</sup> *t*-test method works on the assumption that the data are independent and normally distributed<sup>96</sup>, which is only valid for some variables.

In findchangepts, a changepoint is a time instant at which a statistical property (e.g., the mean, variance, spectral characteristic, etc.) of a given timeseries changes abruptly. The function partitions a timeseries into parts that minimizes the sum of residual squared error of each part from its local statistical property (e.g., mean). The function allows to set a proportionality constant, MinThreshold, corresponding to a fixed penalty added for each changepoint. MinThreshold specifies the minimum improvement in total residual error for each changepoint. The penalty grows linearly with the number of changepoints. Hence, setting a large MinThreshold reduces the number of change points detected due to noise. Not specifying a MinThreshold or a maximum number of changes, can lead in an extreme case to identify a changepoint between for every point and vanishing of the residual error. The findchangepts algorithm was applied in several oceanography and geophysics studies<sup>97–100</sup>.

Here, the changepoint analysis is applied to the gap-filled SLA+ and Chl-a surface coverage timeseries (Figs. 3, 4a, b, 5a–c) using the mean as the chosen statistical property (i.e., detecting most significant abrupt changes in the mean). Changepoints detected in the first or last two years of the timeseries are excluded, as there is not enough information before or after the candidate changepoint to confirm that it is a real abrupt change.

**Cumulative sums of anomalies.** Cumulative sums are an efficient statistical approach that reduce the high frequency noise in the timeseries while objectively detecting changes in slope/trends in

datasets highlighting timing and duration of major (e.g., decadal) changes<sup>101,102</sup>. Here, we use a variant of cumulative sums where original values are normalized to a mean of zero and unit standard deviation (z-scores) before computing the running sum<sup>103</sup>. Normalized cumulative sums segments with increasing slopes represent positive temporal trends (positive anomalies) while segments with decreasing slopes highlight negative temporal trends (negative anomalies), and horizontal segments indicate average conditions<sup>101</sup>. The cumulative sums technique has increasingly been used to determine underlying features of climate variability modes<sup>104</sup> and environmental timeseries<sup>105,106</sup>.

### Data availability

Publicly available satellite and wind datasets were used in this study. The satellite SST, altimetry-derived currents and SLA and primary production are available from the CMEMS<sup>107</sup> data portal (<http://marine.copernicus.eu/services-portfolio/access-to-products/>). In the CMEMS server, the SST data is available under SST\_GLO\_SST\_L4\_REP\_OBSERVATIONS\_010\_011, the SLA and current fields are under SEALEVEL\_GLO\_PHY\_L4\_MY\_008\_047 and the primary production data under OCEANCOLOUR\_GLO\_BGC\_L4\_MY\_009\_104. The satellite Chl-a dataset<sup>108</sup> can be found at the ESA Ocean Colour CCI project website (<https://www.esa-oceancolour-cci.org/>). The ERA-5 wind data<sup>109</sup> is available from the CDS website (<https://cds.climate.copernicus.eu/cdsapp#!/dataset/reanalysis-era5-single-levels-monthly-means?tab=overview>). The JRA55-do wind data<sup>110</sup> is available at <https://climate.mri-jma.go.jp/pub/ocean/JRA55-do/index.html> and [https://climate.mri-jma.go.jp/pub/ocean/JRA55-do/jra55do\\_latest.html](https://climate.mri-jma.go.jp/pub/ocean/JRA55-do/jra55do_latest.html). The IOD timeseries<sup>111</sup> is available at <https://psl.noaa.gov/data/timeseries/DMI>.

### Code availability

The eddy detection algorithm<sup>83</sup> is available online at <https://github.com/chouj/SimpleEddyDetection>. Codes used to calculate the cumulative sums<sup>112</sup> and for the changepoint detection<sup>113</sup> is based on MATLAB R2022a subroutines cumsum.m and findchangepts.m which can be found at <https://uk.mathworks.com/help/signal/ref/cusum.html> and <https://uk.mathworks.com/help/signal/ref/findchangepts.html> respectively. Codes used to produce the main figures are available from the corresponding author on request.

Received: 4 May 2023; Accepted: 13 December 2023;

Published online: 06 January 2024

### References

- Bakun, A. et al. Wiley-Blackwell 103–141 (1998).
- Kushwaha, V. K., Kumar, S. P., Feba, F. & Ashok, K. Findlater jet induced summer monsoon memory in the Arabian Sea. *Sci. Rep.* **12**, 13037 (2022).
- McCreary, J. P., Kohler, K. E., Hood, R. R. & Olson, D. B. A four-component ecosystem model of biological activity in the Arabian Sea. *Prog. Oceanogr.* **37**, 3–4 (1996).
- Chatterjee, A., Kumar, B. P., Prakash, S. & Singh, P. Annihilation of the Somali upwelling system during summer monsoon. *Sci. Rep.* **9**, 7598 (2019).
- deCastro, M., Sousa, M., Santos, F. & Gómez-Gesteira, M. How will Somali coastal upwelling evolve under future warming scenarios? *Sci. Rep.* **6**, 30137 (2016).
- Anderson, D. L. T. The low-level jet as a western boundary current. *Mon. Weather. Rev.* **104**, 907–921 (1976).
- Findlater, J. Interhemispheric transport of air in the lower troposphere over the western Indian Ocean. *Quart. J. R. Meteorol. Soc.* **95**, 400–403 (1969).
- Bakun, A. Climate change and ocean deoxygenation within intensified surface-driven upwelling circulations. *Philos. Trans. R. Soc. A.* <https://doi.org/10.1098/rsta.2016.0327> (2017).
- Schott, F. A., Xie, S. P. & McCreary, J. P. Jr Indian Ocean circulation and climate variability. *Rev. Geophys.* **47**, 1 (2009).
- Varela, R., Álvarez, I., Santos, F., DeCastro, M. & Gómez-Gesteira, M. Has upwelling strengthened along worldwide coasts over 1982–2010? *Sci. Rep.* **5**, 10016 (2015).
- Smith, R. L. Upwelling. *Oceanogr. Mar. Biol. Annu. Rev.* **6**, 11–46 (1968).
- Hastentath, S. & Lamb, P. I. Climatic atlas of the Indian Ocean, part 1. Madison: University of Wisconsin Press, 97 charts, (1979).
- Wiggert, J., Hood, R., Banse, K. & Kindle, J. Monsoon-driven biogeochemical processes in the Arabian Sea. *Prog. Oceanogr.* **65**, 2–4 (2005).
- Lakshmi, S. R., Chatterjee, A., Prakash, S. & Mathew, T. Biophysical interactions in driving the summer monsoon chlorophyll bloom off the Somalia coast. *J. Geophys. Res. Oceans* **125**, e2019JC015549 (2020).
- Vinayachandran, P. N. M. et al. Reviews and syntheses: physical and biogeochemical processes associated with upwelling in the Indian Ocean. *Biogeosci. Discuss.* 1–128 (2021).
- Skeik Heile, A. I. Somali National Report to the Scientific Committee of the Indian Ocean Tuna Commission, IOTC-2018-SC21-NR24. [https://nairobi-convention.org/clearinghouse/sites/default/files/IOTC-2018-SC21-NR24\\_-\\_Somalia.pdf](https://nairobi-convention.org/clearinghouse/sites/default/files/IOTC-2018-SC21-NR24_-_Somalia.pdf) (2018).
- Nootmorn, P., Petpiroon, S. & Maeroh, K. Thai Tuna Longline Fishing in the Indian Ocean from 2000 to 2006". Agriculture and Natural Resources. Bangkok, Thailand, **44**, 1, 61–69. <https://li01.tci-thaijo.org/index.php/anres/article/view/244881> (2010).
- Ardill, J. D. & Sanders, M. J. Proceedings of the Seminar to Identify Priorities for Fisheries Management and Development in the Southwest Indian Ocean. (Albion, Mauritius, September 1991).
- Dueri, S., Bopp, L. & Maury, O. Projecting the impacts of climate change on skipjack tuna abundance and spatial distribution. *Glob. Change Biol.* **20**, 742–753 (2014).
- Schott, F. Monsoon response of the Somali Current and associated upwelling. *Prog. Oceanogr.* **12**, 357–381 (1983).
- Beal, L. M. & Donahue, K. A. The Great Whirl: Observations of its seasonal development and interannual variability. *J. Geophys. Res. Oceans* **118**, 1–13 (2013).
- Melzer, B. A., Jensen, T. G. & Rydbeck, A. V. Evolution of the Great Whirl using an altimetry-based eddy tracking algorithm. *Geophys. Res. Lett.* **46**, 4378–4385 (2019).
- Akuetevi, C. Q. C., Barnier, B., Verron, J., Molines, J. M. & Lecomte, A. Interactions between the Somali Current eddies during the summer monsoon: insights from a numerical study. *Ocean Sci.* **12**, 185–205 (2016).
- Cao, Z. & Hu, R. Research on the interannual variability of the great whirl and the related mechanisms. *J. Ocean Univ. China.* **14**, 17–26 (2015).
- Trott, B., Subrahmanyam, B. & Murty, V. S. N. Variability of the Somali Current and eddies during the southwest monsoon regimes. *Dyn. Atmosph. Oceans* **79**, 43–55 (2017).
- Wang, S. et al. Variability of the great whirl and its impacts on atmospheric processes. *Remote Sensing.* **11**, 322 (2019).
- Brandt, P. et al. Annual Rossby waves in the Arabian Sea from TOPEX/POSEIDON altimeter and in situ data. *Deep Sea Res. II: Top. Stud. Oceanogr.* **49**, 7–8 (2002).
- How oceanographers prevailed over pirates to study the Great Whirl. *Nature* **569**, 310–311 (2019).
- Peng, G. & Olson, D. B. Simulated Somali Coastal Oceanic Response to Various Atmospheric Wind Products during Fall Transitions RSMAS technical report, University of Miami [https://www.researchgate.net/profile/Donald-Olson-3/publication/260402867\\_Simulated\\_Somali\\_Coastal\\_Oceanic\\_Response\\_to\\_Various\\_Atmospheric\\_Wind\\_Products\\_during\\_Fall\\_Transitions/links/0c96053bb2e3d292000000/Simulated-Somali-Coastal-Oceanic-Response-to-Various-Atmospheric-Wind-Products-during-Fall-Transitions.pdf](https://www.researchgate.net/profile/Donald-Olson-3/publication/260402867_Simulated_Somali_Coastal_Oceanic_Response_to_Various_Atmospheric_Wind_Products_during_Fall_Transitions/links/0c96053bb2e3d292000000/Simulated-Somali-Coastal-Oceanic-Response-to-Various-Atmospheric-Wind-Products-during-Fall-Transitions.pdf) (2004).
- Hitchcock, G. L., Key, E. L. & Masters, J. The fate of upwelled waters in the Great Whirl, August 1995. *Deep Sea Research Part II: Topical Studies in Oceanography.* **47**, 1605–1621 (2000). 7–8, pp.
- Dai, L., Han, B., Tang, S., Chen, C. & Du, Y. Influences of the Great Whirl on surface chlorophyll a concentration off the Somali Coast in 2017. *Acta Oceanol. Sin.* **40**, 79–86 (2021).
- Pratik, K., Parekh, A., Karmakar, A., Chowdary, J. S. & Gnanaseelan, C. Recent changes in the summer monsoon circulation and their impact on dynamics and thermodynamics of the Arabian Sea. *Theor. Appl. Climatol.* **136**, 321–331 (2019).
- Kumar, S. P. et al. High biological productivity in the central Arabian Sea during the summer monsoon driven by Ekman pumping and lateral advection. *Curr. Sci.* 1633–1638 (2001).
- Wang, Y., Ma, W., Zhou, F. & Chai, F. Frontal variability and its impact on chlorophyll in the Arabian Sea. *J. Mar. Syst.* **218**, 103545 (2021).
- Watanabe, T. K. et al. Corals reveal an unprecedented decrease of Arabian Sea upwelling during the current warming era. *Geophys. Res. Lett.* **48**, e2021GL092432 (2021).
- Vibhute, A. et al. Decadal variability of tropical Indian Ocean sea surface temperature and its impact on the Indian summer monsoon. *Theor. Appl. Climatol.* **141**, 551–566 (2020).
- Dai, L., Jiang, X., Xia, Y., Zhang, Y. & Du, Y. Impacts of strong positive Indian Ocean Dipole on the generation of the Great Whirl. *Deep Sea Res. I: Oceanogr. Res. Pap.* **189**, 103855 (2022).
- Ng, B. et al. Influence of internal climate variability on Indian Ocean Dipole properties. *Sci. Rep.* **8**, 13500 (2018).
- Ashok, K., Chan, W.-L., Motoi, T. & Yamagata, T. Decadal variability of the Indian Ocean dipole. *Geophys. Res. Lett.* **31**, L24207 (2004).

40. Yuan, Y., Chan, C. L. J., Zhou, W. & Li, C. Decadal and interannual variability of the Indian Ocean Dipole. *Adv. Atmos. Sci.* **25**, 856–866 (2008).
41. Sun, C. et al. Recent acceleration of Arabian Sea warming induced by the Atlantic-western Pacific trans-basin multidecadal variability. *Geophys. Res. Lett.* **46**, 1662–1671 (2019).
42. Du, Y. et al. Thermocline warming induced extreme Indian Ocean dipole in 2019. *Geophys. Res. Lett.* **47**, e2020GL090079 (2020).
43. Effy, J. B., Francis, P. A., Ramakrishna, S. S. V. S. & Mukherjee, A. Anomalous warming of the western equatorial Indian Ocean in 2007: role of ocean dynamics. *Ocean Modelling* **147**, 101542 (2020).
44. Subrahmanyam, B. & Robinson, I. S. Sea surface height variability in the Indian Ocean from TOPEX/POSEIDON altimetry and model simulations. *Mar. Geod.* **23**, 167–195 (2000).
45. Rao, S. A. & Behera, S. K. Subsurface influence on SST in the tropical Indian Ocean: structure and interannual variability. *Dynam. Atmos. Ocean.* **39**, 103–113 (2005).
46. Vinayachandran, P. N., Francis, P. A. & Rao, S. A. Indian Ocean dipole: processes and impacts. *Curr. Trends Sci.* **46**, 569–589 (2009).
47. Chambers, D. P., Tapley, B. D. & Stewart, R. H. Anomalous warming in the Indian Ocean coincident with El Niño. *J. Geophys. Res. Ocean.* **104**, 3035–3044 (1999).
48. Murtugudde, R., McCreary, J. P. Jr. & Busalacchi, A. J. Oceanic processes associated with anomalous events in the Indian Ocean with relevance to 1997–1998. *J. Geophys. Res. Ocean.* **105**, 3295–3306 (2000).
49. Jacobs, Z. L. et al. A major ecosystem shift in coastal East African waters during the 1997/98 Super El Niño as detected using remote sensing data. *Remote Sens.* **12**, 3127 (2020).
50. Xie, S. P., Annamalai, H., Schott, F. A. & McCreary, J. P. Structure and mechanisms of south Indian Ocean Climate Variability. *J. Climate.* **15**, 867–878 (2002).
51. Halo, I. & Raj, R. P. Comparative oceanographic eddy variability during climate change in the Agulhas current and somali coastal current large marine ecosystems. *Environ. Dev.* **36**, 100586 (2020).
52. Rao, S. A., Luo, J. J., Behera, S. K. & Yamagata, T. Generation and termination of Indian Ocean dipole events in 2003, 2006 and 2007. *Climate Dyn.* **33**, 751–767 (2009).
53. Horii, T., Hase, H., Ueki, I. & Masumoto, Y. Oceanic precondition and evolution of the 2006 Indian Ocean dipole. *Geophys. Res. Lett.* **35**, L03607 (2008).
54. Cai, W., Sullivan, A. & Cowan, T. How rare are the 2006–2008 positive Indian Ocean Dipole events? An IPCC AR4 climate model perspective. *Geophys. Res. Lett.* **36**, L08702 (2009).
55. Albert, J., Gulakaram, V. S., Vissa, N. K., Bhaskaran, P. K. & Dash, M. K. Recent warming trends in the Arabian sea: causative factors and physical mechanisms. *Climate.* **11**, 35 (2023).
56. Racault, M. F. et al. Impact of El Niño variability on oceanic phytoplankton. *Front. Mar. Sci.* **4**, 133 (2017).
57. Lenton, T. Tipping points in the climate system. *Weather.* **76**, 325–326 (2022).
58. Sathyendranath, S. et al. ESA ocean colour climate change initiative (Ocean\_Colour\_cci): global ocean colour data products gridded on a geographic projection (all products), version 4.2. Centre for environmental data analysis. <https://catalogue.ceda.ac.uk/uuid/aeae1a19608347f7b802691db6984343> (2020).
59. Jackson, T., Sathyendarnath, S. & Melin, F. An improved optical classification schemes the Ocean Colour Essential Climate Variable and its applications. *Remote Sens. Environ.* **203**, 152–161 (2017).
60. Zhang, C. et al. Bridging between SeaWiFS and MODIS for continuity of chlorophyll-a concentration assessments off Southeastern China. *Remote Sens. Environ.* **102**, 250–263 (2006).
61. IOCCG. Remote sensing of ocean colour in coastal and other optically complex waters. In Reports of the International Ocean Colour Coordinating Group Number 3 (eds. Sathyendranath, Dartmouth, Canada) 140 <https://www.ioccg.org/reports/report3.pdf> (2000).
62. Raitso, D. E., Pradhan, Y., Brewin, R. J., Stenchikov, G. & Hoteit, I. Remote sensing the phytoplankton seasonal succession of the Red Sea. *PLoS ONE* **8**, e64909 (2013).
63. Raitso, D. E. et al. Sensing coral reef connectivity from space. *Sci. Rep.* **7**, 9338 (2017).
64. Antoine, D. & Morel, A. Oceanic primary production: 1. Adaptation of a spectral light- photosynthesis model in view of application to satellite chlorophyll observations. *Glob. Biogeochem. Cycles* **10**, 43–55 (1996).
65. Frouin, R., B. A. Franz & Werdell, P. J. The SeaWiFS PAR product. In Algorithm Updates for the Fourth SeaWiFS Data Reprocessing, S. B. Hooker and E. R. Firestone, Editors, CC NASA/TM-2003-206892. **22**, 46–50 (2003).
66. de Boyer Montégut, C., Madec, G., Fischer, A. S., Lazar, A. & Iudicone, D. Mixed layer depth over the global ocean: An examination of profile data and a profile-based climatology. *J. Geophys. Res. Oceans.* **109**, C12 <https://doi.org/10.1029/2004JC002378> (2004).
67. Garnesson, P., Mangin, A. & Bretagnon, M. Quality Information Document for Ocean Colour Copernicus-GlobColour Products <https://catalogue.marine.copernicus.eu/documents/QUID/CMEMS-OC-QUID-009-101to104-116-118.pdf> (2022).
68. Pujol, M.-I., Taburet, G. & SL-TAC team. Quality information document for sea level TAC - DUACS products <https://catalogue.marine.copernicus.eu/documents/QUID/CMEMS-SL-QUID-008-032-068.pdf> (2023).
69. Pujol, M. I. et al. DUACS DT2014: the new multi-mission altimeter data set reprocessed over 20 years. *Ocean. Sci.* **12**, 1067–1090 (2016).
70. Cipollini, P., et al. Satellite Altimetry in Coastal Regions. in Satellite Altimetry Over Oceans and Land Surfaces. Eds. D. Stammer and A. Cazenave. (Boca Raton, Florida: Taylor & Francis Group), 343–380 (2017).
71. Taburet, G. & Pujol, M.-I. Sea Level Tac - DUACS Products. Quality Information Document. Copernicus Marine Environ. Monitoring Service. Available at: <https://catalogue.marine.copernicus.eu/documents/QUID/CMEMS-SL-QUID-008-032-068.pdf> (2022).
72. Hersbach, H. et al. ERA5 monthly averaged data on single levels from 1979 to present. Copernicus Climate Change Service (C3S) Climate Data Store (CDS), <https://doi.org/10.24381/cds.fl7050d7> (2019).
73. Gill, A. E. Atmosphere-Ocean Dynamics. Academic, San Diego, Calif. (1982).
74. Kobayashi, S. et al. The JRA-55 reanalysis: general specifications and basic characteristics. *J. Meteor. Soc. Jpn* **93**, 5–48 (2015).
75. Tsujino, H. et al. JRA-55 based surface dataset for driving ocean-sea ice models (JRA55-do). *Ocean Modelling.* **130**, 79–139 (2018).
76. Nencioli, F., Dong, C., Dickey, T., Washburn, L. & McWilliams, J. C. A. Vector geometry-based eddy detection algorithm and its application to a high-resolution numerical model product and high-frequency radar surface velocities in the southern California bight. *J. Atmos. Oceanic Technol.* **27**, 564–579 (2010).
77. Yuan, D., Han, W. & Hu, D. Anti-cyclonic eddies northwest of Luzon in summer-fall observed by satellite altimeters. *Geophys. Res. Lett.* **34**, L13610 (2007).
78. Zhang, W. Z., Xue, H., Chai, F. & Ni, Q. Dynamical processes within an anticyclonic eddy revealed from Argo floats. *Geophys. Res. Lett.* **42**, 2342–2350 (2015).
79. Chaigneau, A., Eldin, G. & Dewitte, B. Eddy activity in the four major upwelling systems from satellite altimetry (1992–2007). *Prog. Oceanogr.* **83**, 117–123 (2009).
80. Chaigneau, A., Gizolme, A. & Grados, C. Mesoscale eddies off Peru in altimeter records: identification algorithms and eddy spatio-temporal patterns. *Prog. Oceanogr.* **79**, 2–4 (2008).
81. Chelton, D. B., Schlax, M. G. & Samelson, R. M. Global observations of nonlinear mesoscale eddies. *Prog. Oceanogr.* **91**, 167–216 (2011).
82. Xu, C., Shang, X. D. & Huang, R. Horizontal eddy energy flux in the world oceans diagnosed from altimetry data. *Sci. Rep.* **4**, 5316 (2014).
83. Xu, C., Zhai, X. & Shang, X. D. Work done by atmospheric winds on mesoscale ocean eddies. *Geophys. Res. Lett.* **43**, 23 (2016).
84. <https://github.com/chouj/SimpleEddyDetection> (2022). Chi SimpleEddyDetectionGitHub. Retrieved May 11.
85. Okubo, A. Horizontal dispersion of floatable particles in the vicinity of velocity singularities such as convergences. *Deep Sea Res. Oceanogr. Abstracts.* **17**, 445–454 (1970).
86. Weiss, J. The dynamics of enstrophy transfer in two-dimensional hydrodynamics. *Physica D: Nonlinear Phenomena.* **48**, 273–294 (1991).
87. Vic, C., Roulet, G., Carton, X. & Capet, X. Mesoscale dynamics in the Arabian Sea and a focus on the Great Whirl life cycle: a numerical investigation using ROMS. *J. Geophys. Res. Oceans* **119**, 6422–6443 (2014).
88. Uz, B. M. What causes the sporadic phytoplankton bloom southeast of Madagascar? *J. Geophys. Res. Oceans* **112**, C09010 (2007).
89. Dilmahamad, A. F., Penven, P., Aguiar-González, B., Reason, C. J. C. & Hermes, J. C. A new definition of the South-East Madagascar Bloom and analysis of its variability. *J. Geophys. Res. Oceans* **124**, 1717–1735 (2019).
90. Jacobs, Z. L. et al. Shelf-break upwelling and productivity over the North Kenya Banks: the importance of large-scale ocean dynamics. *J. Geophys. Res. Oceans.* **125**, e2019JC015519 (2020).
91. Hammond, M. L., Jebri, F., Srokosz, M. & Ekaterina, P. Automated detection of coastal upwelling in the Western Indian Ocean: Towards an operational “Upwelling Watch” system. *Front. Mar. Sci.* **9** <https://www.frontiersin.org/articles/10.3389/fmars.2022.950733> (2022).
92. Killick, R., Fearnhead, P. & Eckley, I. A. Optimal detection of change points with a linear computational cost. *J. Am. Stat. Assoc.* **107**, 1590–1598 (2012).
93. Beaulieu, C. & Killick, R. Distinguishing trends and shifts from memory in climate data. *J. Clim.* **31**, 9519–9543 (2018).
94. Rodionov, S. N. A sequential algorithm for testing climate regime shifts. *Geophys. Res. Lett.* **31**, L09204 (2004).
95. Ruggieri, E. A. Bayesian approach to detecting change points in climatic records. *Int. J. Climatol.* **33**, 520–528 (2013).
96. Room, A. H., Franco-Gaviria, F. & Urrego, D. H. rshift STARS manual - regime shift analysis for paleoecological data v2.1.1 <https://cran.r-project.org/web/packages/rshift/vignettes/STARSmanual.pdf> (2022).

97. Dell, R., Carr, R., Phillips, E. & Russell, A. Response of glacier flow and structure to proglacial lake development and climate at Fjallsjökull, south-east Iceland. *J. Glaciol.* **65**, 321–336 (2019).
98. Opdal, A. F. et al. Unclear associations between small pelagic fish and jellyfish in several major marine ecosystems. *Sci. Rep.* **9**, 2997 (2019).
99. Almoth-Rosell, E. et al. A Regime Shift Toward a More Anoxic Environment in a Eutrophic Sea in Northern Europe. *Frontiers in Marine Science*. **8** <https://www.frontiersin.org/articles/10.3389/fmars.2021.799936> (2021).
100. Gilarranz, L. J., Narwani, A., Odermatt, D., Siber, R. & Dakos, V. Regime shifts, trends, and variability of lake productivity at a global scale. *Proc. Natl. Acad. Sci. USA* **119** <https://doi.org/10.1073/pnas.2116413119> (2022).
101. Briceno, H. O. & Boyer, J. N. Climatic controls on phytoplankton biomass in a sub-tropical estuary, Florida Bay, USA. *Estuar. Coast.* **33**, 541–553 (2010).
102. Regier, P., Briceno, H. & Boyer, J. N. Analyzing and comparing complex environmental time series using a cumulative sums approach. *MethodsX*. **6**, 779–787 (2019).
103. Taylor, A., Allen, J. & Clark, P. Extraction of a weak climatic signal by an ecosystem. *Nature*. **416**, 629–632 (2002).
104. Martinez, E., Raitos, D. E. & Antoine, D. Warmer, deeper, and greener mixed layers in the North Atlantic subpolar gyre over the last 50 years. *Glob. Change Biol.* **22**, 604–612 (2016).
105. Liuzzo, L., Bono, E., Sammartano, V. & Freni, G. Long-term temperature changes in sicily, southern Italy. *Atmos. Res.* **198**, 44–55 (2017).
106. Gittings, J. A., Raitos, D. E., Krokos, G. & Hoteit, I. Impacts of warming on phytoplankton abundance and phenology in a typical tropical marine ecosystem. *Sci. Rep.* **8**, 2240 (2018).
107. CMEMS, <http://marine.copernicus.eu/services-portfolio/access-to-products/>.
108. OC-CCI version 5, <http://www.esa-oceancolour-cci.org/>.
109. CDS ERA-5 wind data, <https://cds.climate.copernicus.eu/cdsapp#!/dataset/reanalysis-era5-single-levels-monthly-means?tab=overview>.
110. JRA55-do wind data, <https://climate.mri-jma.go.jp/pub/ocean/JRA55-do/index.html> and [https://climate.mri-jma.go.jp/pub/ocean/JRA55-do/jra55do\\_latest.html](https://climate.mri-jma.go.jp/pub/ocean/JRA55-do/jra55do_latest.html).
111. IOD HadISST data v1.1 version, <https://psl.noaa.gov/data/timeseries/DMI>.
112. Cusum code, <https://uk.mathworks.com/help/signal/ref/cusum.html>.
113. Findchangepts code, <https://uk.mathworks.com/help/signal/ref/findchangepts.html>.

## Acknowledgements

The study was supported by the Global Challenges Research Fund (GCRF) under NERC grant NE/P021050/1 in the framework of the SOLSTICE-WIO project (<https://www.solstice-wio.org/>) as well as the UK National Capability project FOCUS (<https://noc.ac.uk/projects/focus>) under grant NE/X006271/1. A.S.-F. was supported by the NEW NORMAL project (<https://noc.ac.uk/projects/new-normal>) under NERC grant NE/W003813/1.

## Author contributions

F.J., M.S., and D.E.R. conceived the ideas and designed the methodology. F.J. wrote the original draft and led the coding and analysis. Z.L.J. and E.P. contributed to the analysis of the results and revising the paper. A.S.-F. conducted analysis of local wind forcing. E.P. was responsible for the project direction and funding. All authors made substantial contributions to the drafts and the interpretation of the results and approved the final manuscript.

## Competing interests

The authors declare no competing interests.

## Additional information

**Supplementary information** The online version contains supplementary material available at <https://doi.org/10.1038/s43247-023-01183-9>.

**Correspondence** and requests for materials should be addressed to Fatma Jebri.

**Peer review information** *Communications Earth & Environment* thanks Abhishek Chatterjee and the other, anonymous, reviewer(s) for their contribution to the peer review of this work. Primary Handling Editors: Jennifer Veitch and Clare Davis. Peer reviewer reports are available.

**Reprints and permission information** is available at <http://www.nature.com/reprints>

**Publisher's note** Springer Nature remains neutral with regard to jurisdictional claims in published maps and institutional affiliations.



**Open Access** This article is licensed under a Creative Commons Attribution 4.0 International License, which permits use, sharing, adaptation, distribution and reproduction in any medium or format, as long as you give appropriate credit to the original author(s) and the source, provide a link to the Creative Commons licence, and indicate if changes were made. The images or other third party material in this article are included in the article's Creative Commons licence, unless indicated otherwise in a credit line to the material. If material is not included in the article's Creative Commons licence and your intended use is not permitted by statutory regulation or exceeds the permitted use, you will need to obtain permission directly from the copyright holder. To view a copy of this licence, visit <http://creativecommons.org/licenses/by/4.0/>.

© The Author(s) 2024